Beneficial effect of Na_2CO_3 additions on the thermoelectric performance of melt-route Cu_2Se

Sheik Md Kazi Nazrul Islam, Md Rezoanur Rahman, Al Jumlat Ahmed, Frank Fei Yun, David L. Cortie, Xiaolin Wang*, Michael B. Cortie*

Sheik Md Kazi Nazrul Islam, Michael B. Cortie
School of Mathematical and Physical Sciences, University of Technology Sydney, Broadway, NSW 2007, Australia.
E-mail: michael.cortie@uts.edu.au

Md Rezoanur Rahman, Al Jumlat Ahmed, Frank Fei Yun, David L. Cortie, Xiaolin Wang
Institute for Superconducting and Electronic Materials, Australian Institute for Innovative Materials, University of Wollongong, North Wollongong, NSW 2500, Australia.
E-mail: xiaolin@uow.edu.au

Keywords: thermoelectric, melt-route, copper selenide, sodium doping, figure-of-merit

High-performance thermoelectric materials require simultaneous reduction of thermal conductivity and electrical resistivity, amongst other criteria. Here we show that the introduction of Na_2CO_3 into the melt-route fabrication process for the well-known thermoelectric Cu_2Se has a beneficial and surprisingly strong effect. Electrical conductivity is increased and thermal conductivity is decreased but there is only a small change in Seebeck coefficient. A higher power factor of 12.6 $\mu W \cdot cm^{-1} \cdot K^{-2}$ is achieved *vs* 8.8 $\mu W \cdot cm^{-1} \cdot K^{-2}$ for standard Cu_2Se. A very high value of zT of 2.3 is obtained at 804 K vs 1.1 for standard Cu_2Se. Density functional theory calculations suggest that Na and O doping of the Cu_2Se may be responsible for the improvement in electrical conductivity. The 34% reduction in thermal conductivity for the material to which Na_2CO_3 has been added is likely due to a high density of defects causing scattering of phonons.

1. Introduction

Thermoelectric semiconductors can be harnessed to convert heat flow into electric power. There is continuous interest in these compounds since they can produce energy from quite low grade heat sources. For example, a thermoelectric generator can convert heat in an automobile exhaust to drive the vehicle's electrical systems[1, 2] or, if worn in close contact with human skin, it could harvest sufficient energy to drive some low-power medical or consumer device.[3] There are many factors that determine the usefulness of a thermoelectric system, including the Carnot efficiency. The latter places an absolute upper limit on what is possible in terms of energy conversion.

It is common to compare the efficacy of thermoelectric materials using a figure-of-merit, zT, computed as

$$zT = \frac{\sigma S^2 T}{\kappa} \quad (1)$$

where $\sigma(T)$ is the electrical conductivity, $S(T)$ the Seebeck coefficient, T the absolute temperature and $\kappa(T)$ the thermal conductivity. In the limit, if $zT=\infty$ then the device would operate at the Carnot efficiency, η,

$$\eta = 1 - \frac{T_{cold}}{T_{hot}} \quad (2)$$

Actual figures-of-merit are quite modest however and, for example, a device with zT of 2 and ΔT of 1000 K could only operate at about 40% of its 72% Carnot efficiency[1] (to give an overall conversion efficiency of about 30%). This can be contrasted to a large-scale state-of-the-art coal-fired power station which can reach about 70% of its Carnot limit at 1000 K[1] (yielding an overall conversion efficiency of about 50%). In general, however, hot-side temperatures are lower than 1000 K which reduces the Carnot limit considerably. For example, a recent publication claimed a record-high overall conversion efficiency of 7.3% for

a Mg_3Sb_2/MgAgSb module.[4] In this case it was operated between 593 and 278 K. The Carnot efficiency for these temperatures would be 53% so the device only reached 13% of the theoretically attainable limit.

The use of *zT* as a measure of potential efficacy is also complicated slightly by the fact that it varies with temperature whereas, in contrast, the device operating temperature is usually externally imposed by the technological system being considered, and therefore cannot be changed. For example, in the motor vehicle exhaust scenario the 'hot' temperature could be 670 to 920 K[2] whereas in the wearable medical device instance it would be about 310 K (i.e. body temperature). The 'cold' temperature in both instances would be the ambient, *i.e.* about 290 to 300 K. The implication of this is that a thermoelectric material may have a competitive *zT* for one type of application but not for another.

Examination of Equation (1) indicates that *zT* can be increased by maximizing electrical conductivity and minimizing thermal conductivity. Since heat flow in solids is carried by phonons, increasing resistance to phonon mobility is a useful strategy. For example, recent studies on Cu_2Se (a *p*-type thermoelectric compound that has been known since at least the mid-1960s)[5] have shown that the superionic nature of its high temperature β phase (meaning that the Cu atoms are in a liquid-like state)[6, 7] suppresses some vibrational modes and enables zT values of as high as 1.5 at 1000 K to be achieved.[6] On top of this, incorporating carbon nanotubes, graphene, graphite, copper oxide, carbon dots or other heterogeneities into the microstructure of Cu_2Se can reduce heat conduction further by way of additional scattering or attenuating of the phonons.[8, 9, 10] Values of zT for Cu_2Se in excess of 2.4 at 870 K have been obtained by these means.[11] Another strategy requires the operating temperature of the device to align with the $\alpha \rightarrow \beta$ phase transformation of Cu_2Se (350 to 410 K depending on exact composition). This enhances zT in that range,[12] with values of ~2.3 (or even higher) claimed.[13, 14]

Alloying of thermoelectrics with a substitutional third element has also been extensively explored over the years. Additions of Ag,[5, 15] Sn,[9] In,[16, 17] I,[13] B,[18] Fe,[17] Ni,[17] Mn,[17] Zn,[17] Sm,[17] Li,[19] S,[20] Te[21] and Na[22-24] have been investigated in the case of $Cu_{2-x}Se$. At first sight Na would seem to be an improbable proposition for $Cu_{2-x}Se$: as an element it is considerably less electronegative than Cu (0.93 vs 1.90, in Pauling units), and its ionic radius as a monovalent ion (116 vs 91 pm) is significantly larger than that of Cu^+ (these are Shannon[25] six-coordinated crystal radii for 1^+ ions). In contrast, it has long been known that doping Pb chalcogenides with Na is beneficial because it renders them *p*-type[26-28] (due to Na contributing only one electron compared to the two of Pb). The limit of solubility is of the order of an atomic percent, so greater amounts than that must necessarily create a heterogeneous microstructure.[27] The latter may also be beneficial for thermoelectric applications because the associated microstructural defects on grain boundaries and dislocations reduce heat conduction.[27, 28]

$Cu_{2-x}Se$ is already *p*-type[12] and substituting a Na (one free electron) for a Cu (one free electron) should not, to a first approximation, change the carrier density that much. Nevertheless, three independent reports on adding Na to hydrothermally-prepared Cu_2Se point to improved properties.[22-24] Increased scattering of phonons, and hence decreased thermal conductivity, seemed to be the main benefit reported in these previous papers. In fact, Sudha et al.[22] and Jin et al.[24] reported that additions of Na substituted for Cu slightly reduced carrier concentration and electrical conductivity (relative to pure $Cu_{2-x}Se$) which would be undesired outcomes. The reduction in carrier concentration was said to be the result of electron injection from the Na, resulting in reduced hole concentration.[24] However, whereas Jin et al.[24] reported a reduction in mobility with addition of Na, Sudha et al.[22] found an increase in mobility. In both cases the amount of Na added was not more than 5 at.%. Zhu et

al.[23] added up to 1.3 at.% Na in the compound $Cu_{2-x}Na_xSe$ and found it caused reduction in thermal conductivity of up to a factor of 2. They attributed this change to the formation of micro-porosity as the result of the Na addition. There was a marked improvement in *zT* in the latter case, for example from about 1.5 (no Na) to 2.1 (about 1.3 at. % Na) at 973 K.

The $Cu_{2-x}Na_xSe$ in all three references cited above was made by the *hydrothermal route*, followed by some solid-state heat treatment. In the present work we examine the effect of incorporating Na_2CO_3 into *melt-processed* Cu_2Se. We will propose that partial decomposition of the carbonate at elevated temperatures results in the transfer of some Na and, possibly, O into the Cu_2Se lattice. Our aim is to determine whether this novel source of Na and O can confer benefits to melt-route material and, if so, to elucidate the mechanism of improvement.

2. Results

Room temperature laboratory powder X-ray diffraction patterns for the pure Cu_2Se and the samples to which Na_2CO_3 had been added are shown in **Figure 1**a. The patterns match with the low temperature monoclinic form of Cu_2Se (PDF 04-018-3523, C2/c S.G. #15, designated LT-Cu_2Se or α-Cu_2Se in the phase diagram literature).[29, 30] Rietveld refinement of all the room temperature laboratory patterns are shown in Figure 1b (the refined parameters are provided in Supporting Information **Table S1**). The lattice parameters and volume are plotted in Figure 1c. These inflation of the lattice with additions of Na_2CO_3 indicates that the crystal structure of the α-Cu_2Se is increasingly effected by the incorporation of a third element in solid solution.

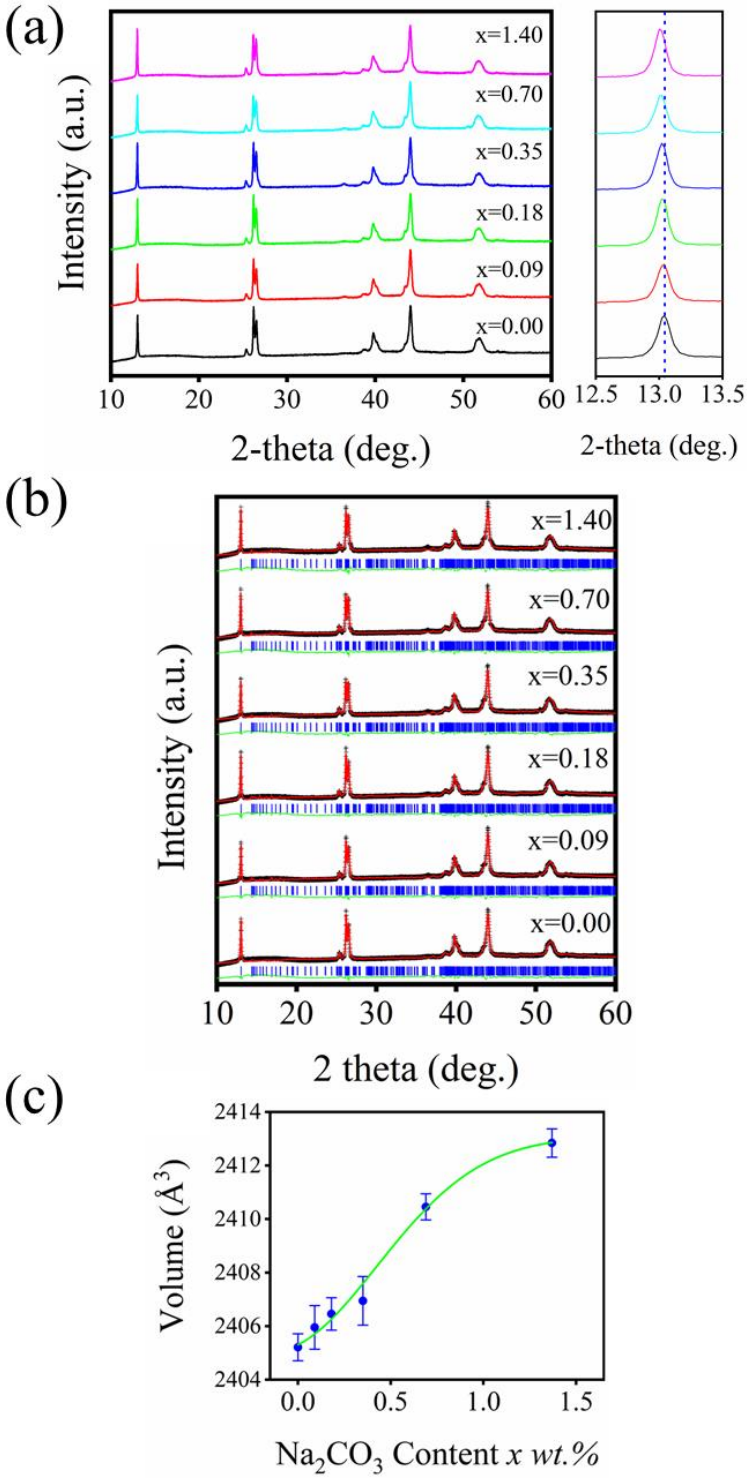

Figure 1. a) Room temperature powder x-ray diffraction pattern of Cu_2Se-x wt. % Na_2CO_3 samples (x = 0, 0.09, 0.18, 0.35, 0.70, and 1.40). Right-hand side is the enlarged view of a selected region; b) Refined RT XRD patterns (+ data points,− calculation line, | marker points, − difference line; (c) volume ($Å^3$) as a function of Na_2CO_3 content. The refined parameters are provided in Table S1.

In order to further investigate the effect of the Na_2CO_3 addition, we have carried out variable temperature synchrotron XRD analyses. Iso-intensity images of the pure and the 1.40 wt.% Na_2CO_3 samples shown in **Figure 2**a-b from room temperature to 774 K. The peaks of the α-phase at around 5° and ~15° gradually weaken and then disappear with increase in temperature as the samples transform to the high temperature cubic phase (Fm-3m (#225), normally designated β-Cu_2Se or HT-Cu_2Se). Normalized area under selected peaks of α-phase are shown in Figure 2c for the pure and 1.40 wt.% Na_2CO_3 materials as a function of temperature. It is evident that addition of 1.40 wt.% Na_2CO_3 has caused the α→β phase transition to be shifted about 30 K upwards in temperature. This is also evident in the DSC data (Supporting Information, **Figure S1**). Since the processing of the samples has been identical (except for the different Na_2CO_3 additions) this most probably indicates that some change in the composition of the Cu_2Se phase has taken place. Rietveld refinement of the temperature-dependent XRD patterns of pure and 1.40 wt.% Na_2CO_3 samples are shown in Figure 2d-e. The refined parameters (**Table S2**) and lattice parameters as a function of temperature (Figure 2f) reveal an increase in lattice parameter of the β-Cu_2Se with the addition of Na_2CO_3. This is yet further evidence that some change in the composition of the Cu_2Se has taken place.

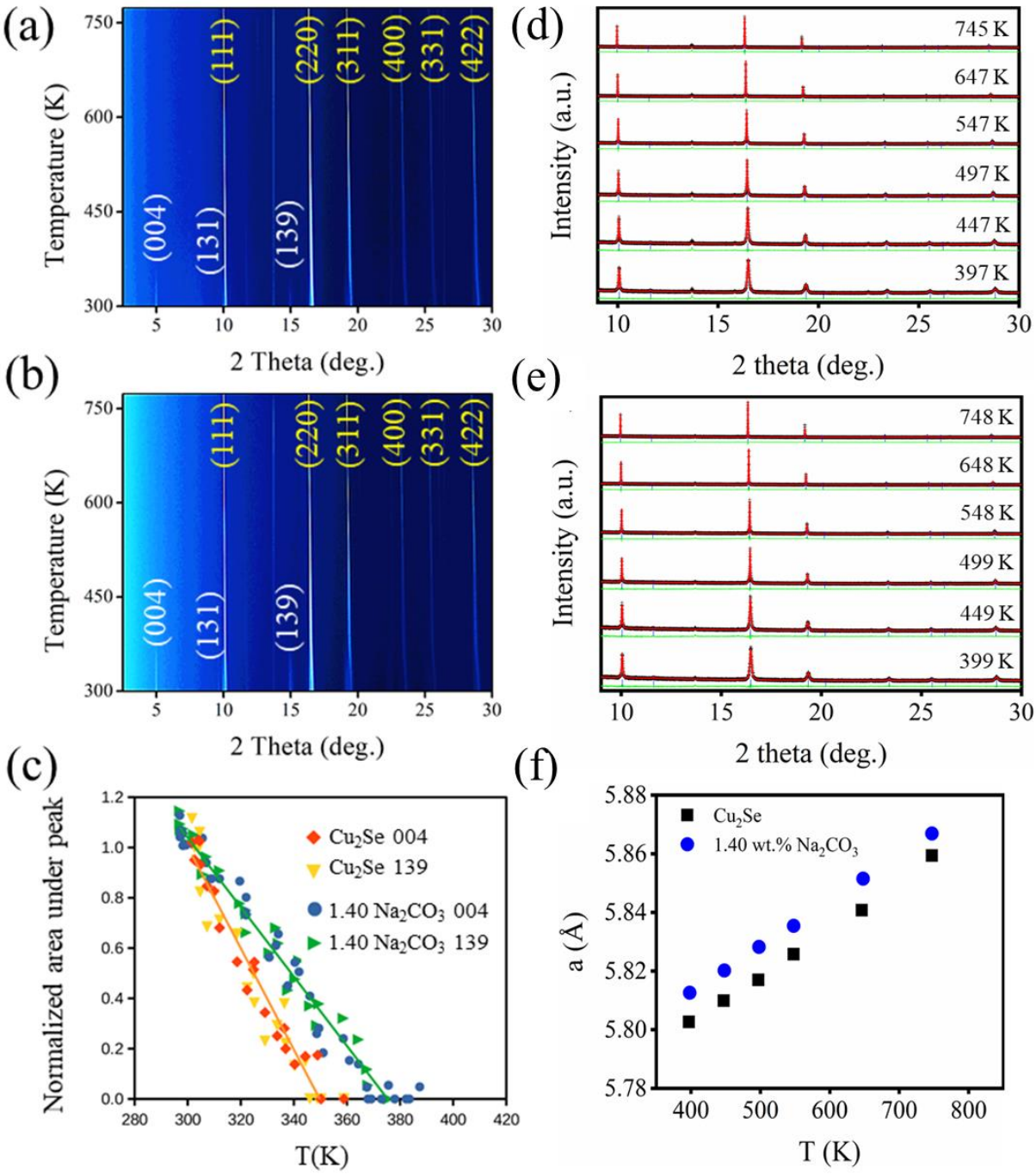

Figure 2. Iso-intensity images of the a) pure Cu_2Se and b) 1.40 wt.% Na_2CO_3 sample. The wavelength is 0.58973 Å; c) Normalized area under selected peaks of Cu_2Se alpha phase of the pure and 1.40 wt.% Na_2CO_3 Cu_2S with temperature. d,e) Rietveld refinements of synchrotron powder diffraction patterns of Cu_2Se and 1.40 wt.% Na_2CO_3 incorporated Cu_2Se (+ data points,– calculation line, | marker points, – difference line); f) Lattice parameters for high temperature forms of pure and 1.40 wt.% Na_2CO_3 Cu_2Se.

We examined the effect of different levels of Na_2CO_3 addition in $Cu_{2-x}Se$ through their influence on electrical conductivity (σ), Seebeck coefficient (S), thermal conductivity (κ), and figure of merit (zT). The temperature dependence of σ as a function of Na_2CO_3 addition (0.09, 0.18, 0.35, 0.70, and 1.40 wt.%) in the temperature ranges from 355 K to 981 K is shown in **Figure 3**a. We observed that electrical conductivity increases with increasing Na_2CO_3 addition. The electrical conductivity of ~890 $S \cdot cm^{-1}$ at 458 K for the 1.4 wt.% Na_2CO_3 samples is about 70% higher than that of pure Cu_2Se. This result is amongst the highest values previously reported for Cu_2Se at the same temperature.[6, 31, 32] To understand the enhancement of σ, Hall carrier concentration (p) and Hall carrier mobility (μ_H) were measured by the van der Pauw method is shown in Figure 3b. We found from the Hall effect measurements that the overall enhancement of σ is primarily due to the improvement of hole carrier concentration.

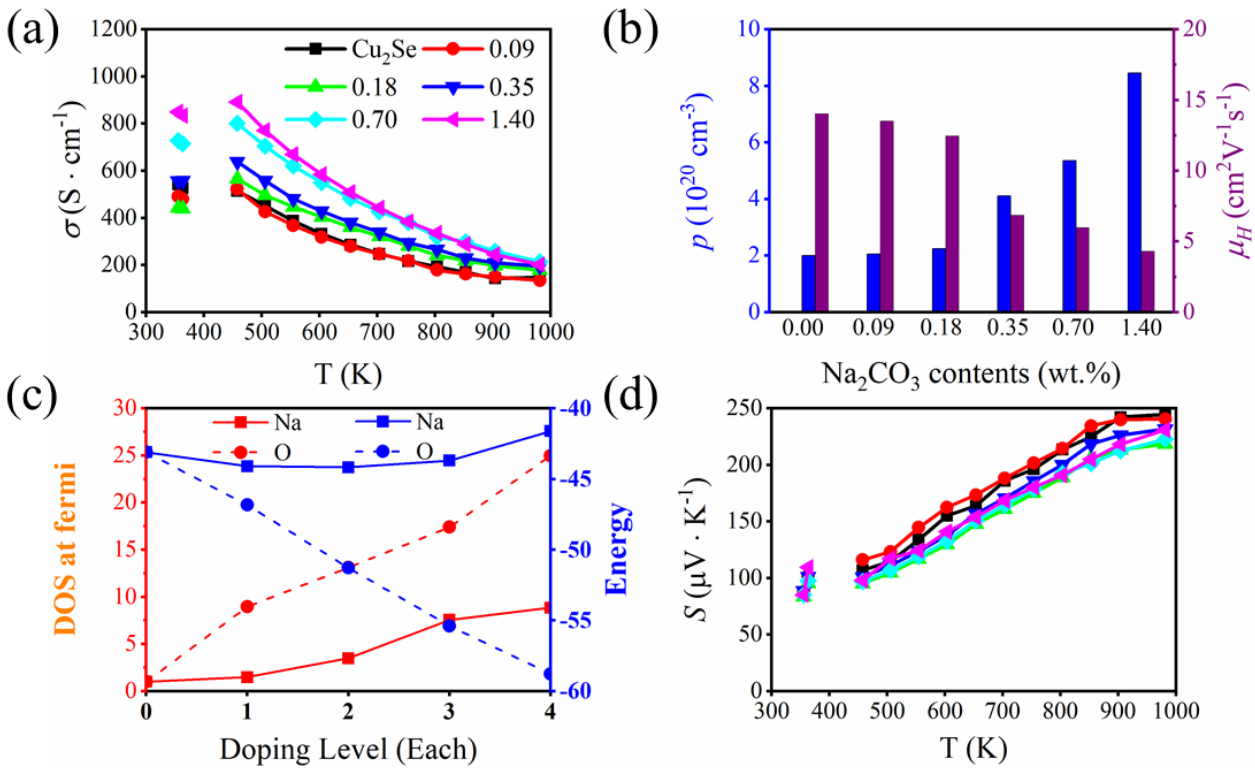

Figure 3. Temperature dependent transport properties of the Cu_2Se-x wt. % Na_2CO_3 samples (x = 0, 0.09, 0.18, 0.35, 0.70, and 1.40). (a) Electrical conductivity (σ); (b) carrier concentration (p) and carrier mobility (μH); (c) Sodium and oxygen doping level dependence density of states (DOS). The Fermi energy (left axis) and the binding energy (right axis); (d) Seebeck coefficient (S). Properties in the two phase $\alpha+\beta$ region are not shown.

We further investigated the effect of Na_2CO_3 in Cu_2Se by density functional theory calculations in order to understand the system's electronic density of states (DOS), which in turn, affects its electrical conductivity. Before discussing the DOS, however, some further comments about the Cu_2Se crystal structure might be helpful. At temperatures above about 400 K $Cu_{2-x}Se$ has a cubic structure but with the Cu ions somewhat mobile. This is an example of a 'superionic' phase. Upon cooling below 400 K,[6, 33] it undergoes a reversible structural phase transition into the low-temperature α-Cu_2Se mentioned previously.[29] In the cubic structure, Se^{2-} anions are closely packed into a face-centered cubic (fcc) framework with a statistical distribution of $4(2 - x)$ Cu^+ cations in the four octahedral and eight tetrahedral interstitial sites. Therefore, the average site occupancy factor, $f = 4(2 - x)/12$, in the $Cu_{2-x}Se$ structure depends on the degree of off-stoichiometry, x, with the maximum occupancy factor of 2/3 for the stoichiometric composition. This large proportion of intrinsic vacancies is believed to be responsible for the *p*-type character as well as the superionic liquid-like behavior of Cu^+ ions in the $Cu_{2-x}Se$ structure.[6] Therefore, to understand the effect on σ by Na_2CO_3 additions to Cu_2Se, we have performed density of state and electronic structure calculations of the pure Cu_2Se and 11 different possible variations shown in **Figure S2**, **Figure S3** and **Figure S4**. It can be seen that pure Cu_2Se is a zero-gap material,[34] which is in good agreement with what has been reported in Råsander et al.[35] A variety of both Na and O doping configurations were considered for both substitutional and interstitial states. Additionally, defect states containing either Cu or Se vacancies were considered. DOS results show that, due to low DOS at the Fermi energy, the contribution of free electrons originating from *s*, *p*, and *d* orbitals are similarly near zero. When oxygen doping is incorporated into the structure, there is an increase in the binding energy, and simultaneously an increase in the density of state at the Fermi energy from oxygen *p* orbital states shown in Figure 3c. In contrast, Na doping causes a smaller increase in the DOS at Fermi energy. This doping coincides with a lowering of the binding energy. This is evidence for the fact that O doping is more energetically favorable due to the more favorable energy of the Cu-O bond. (We consider the possible chemical reactions responsible for

the presumed doping later in this paper.) Combinations of Na, O doping, Na doping/O substitution, O doping/Na substitution, and O substitution all increase the DOS at Fermi energy. As a result of this increase in the DOS at the Fermi level, i.e. the number of free carriers, there is an increase in electrical conductivity. These expectations are in agreement with our experimental observations.

The improvement of electrical conductivity often causes a drop of Seebeck coefficient (*S*). The temperature-dependent *S* for the pure Cu_2Se is compared to that of materials made with Na_2CO_3 additions in Figure 3d. We observed that increasing the content of Na_2CO_3 in Cu_2Se slightly decreases *S* while increasing σ in the whole measured temperature range. Here, all samples exhibit positive Seebeck coefficients (S) in line with the fact that holes are the major charge carriers. The overall Seebeck coefficients reaches between 100 and 250 $\mu V.K^{-1}$ from 458 K to 981 K. A comparison of the calculated power factors, $PF = \sigma S^2$ for the pure Cu_2Se and samples to which Na_2CO_3 had been added is interesting (**Figure S5**). The PF values for the pure Cu_2Se sample observed before and after the phase transition range from $5 - 8.8\ \mu W \cdot cm^{-1} \cdot K^{-2}$ which is comparable with previously reported results.[31, 36] There was an overall enhancement of PF observed for the samples made with Na_2CO_3. The highest result of $12.6\ \mu W \cdot cm^{-1} \cdot K^{-2}$ at 704 K was obtained for the 1.40 wt.% Na_2CO_3 sample. This result is ~47% higher than for the pure Cu_2Se sample.

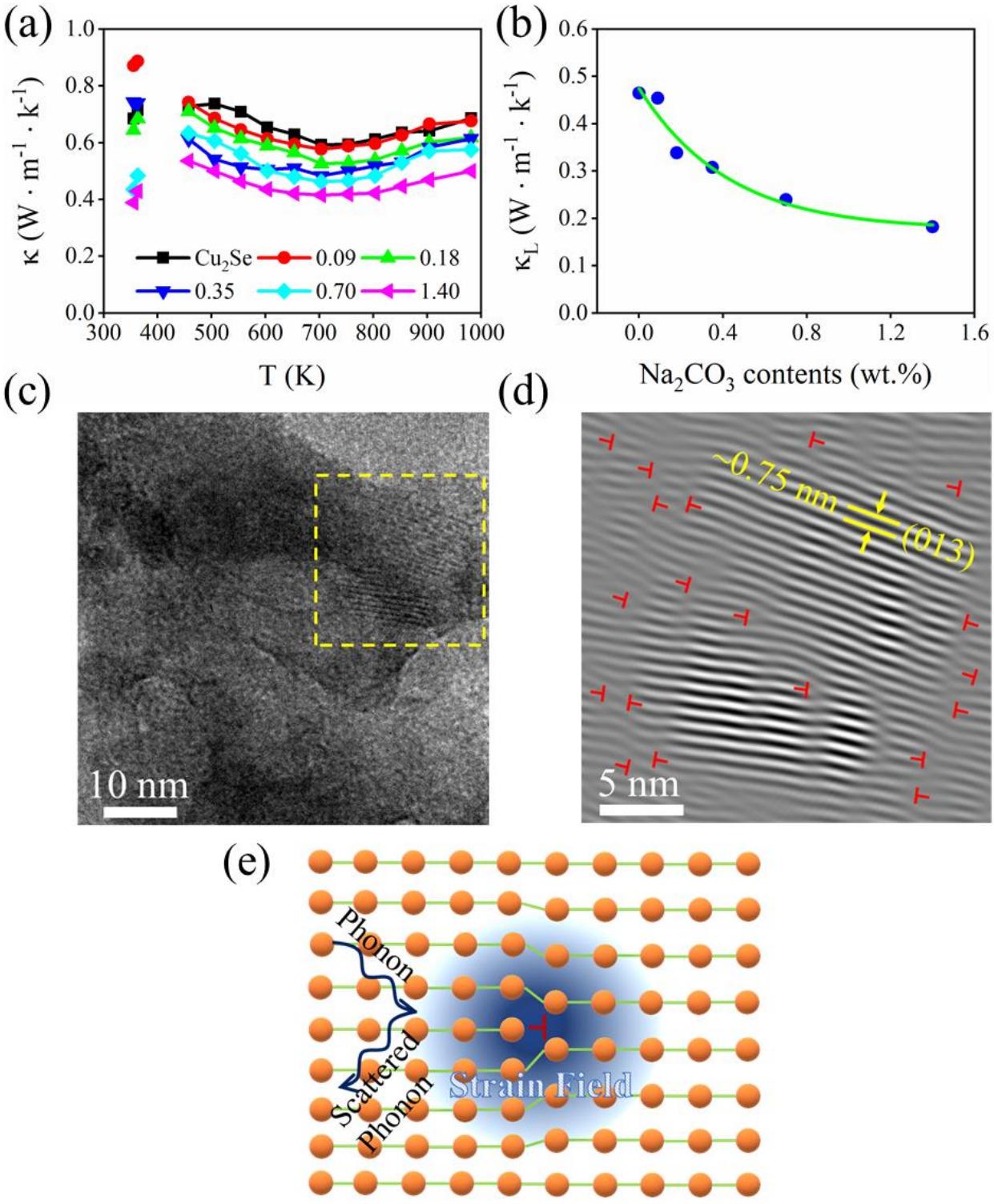

Figure 4. Temperature dependence of the thermal transport properties of pure Cu_2Se and Cu_2Se made with Na_2CO_3 additions. (a) Thermal conductivity (κ); (b) Lattice thermal conductivity (κ_L) for the Cu_2Se/*x* wt% Na_2CO_3 (*x* = 0, 0.09, 0.18, 0.35, 0.70, and 1.40 wt.%) at 980 K; (c) TEM image of a sample made with 1.40 wt.% Na_2CO_3; (b) Inverse FFT image of the selected dash yellow square region of Figure 4(c) clearly identifying the dislocations; (c) Schematic diagram of phonon transport mechanism in Cu_2Se.[39]

Field emission scanning electron microscope (FE-SEM) EDS analyses of the pure and Na_2CO_3 - containing Cu_2Se are shown in **Figure S6**. All the samples were found to be dense with no observed porosity.

The temperature-dependent thermal conductivity (κ) of the pure Cu_2Se and samples to which Na_2CO_3 had been added are shown in **Figure 4a**. We observed that thermal conductivity decreases with the higher amount of Na_2CO_3. The lowest κ observed is for the 1.40 wt.% Na_2CO_3 and this is ~34% lower than pure Cu_2Se. The lattice thermal conductivity (κ_L), shown in Figure 4b, has been calculated by subtracting the carrier part (κ_c) from total κ. Here, κ_c is calculated by the Wiedermann-Franz Law ($\kappa_c = L.\sigma.T$, where L is a constant known as the Lorenz number, L= 1.6×10^{-8} $V^2 \cdot K^{-2}$).[6, 37] The κ_L value observed significantly decreases with the amount of Na_2CO_3 used. It is lower than for most of the previously reported polycrystalline samples.[28, 31, 38] A TEM image of the sample containing 1.40 wt.% Na_2CO_3 is shown in Figure 4c. The inverse FFT image of the selected dash yellow square region of Figure 4c clearly identifies the dislocations (indicated by red arrow) shown in Figure 4d. A schematic diagram of the mechanism of phonon transport in Cu_2Se is shown in Figure 4e.[39], [40] Although a dislocation is shown as the scattering center, it could also have been any other defect such as a vacancy or a Na atom. The dislocations, vacancies, oversized Na atoms and grain boundaries can each induce extended strain fields and in turn result in phonon scattering.

Figure 5a shows the temperature-dependent thermoelectric figure-of-merit (zT) for the pure Cu_2Se and samples to which Na_2CO_3 has been added. The result shows that highest value of zT=2.3 at 804 K was obtained for samples to which 1.40 wt.% Na_2CO_3 had been added. This is around 100% higher than the pure Cu_2Se sample. Figure 5b shows the calculated efficiency and measured according to the formula[41]

$$\eta_{max} = \frac{\Delta T}{T_{hot}} \frac{(1+zT_{avg})^{1/2} - 1}{(1+zT_{avg})^{1/2} + \frac{T_{cold}}{T_{hot}}} \quad (3)$$

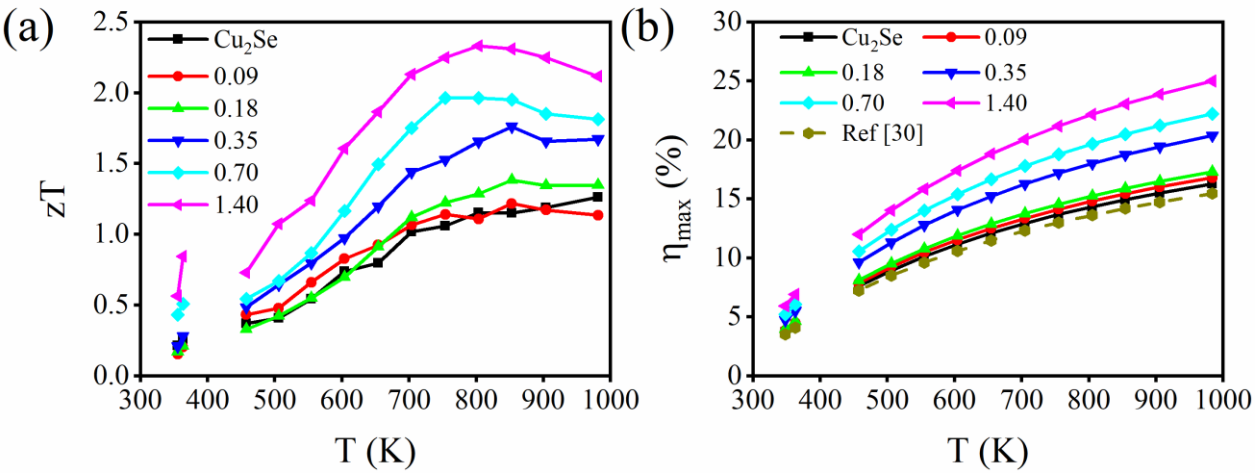

Figure 5. Temperature dependence of (a) figure-of-merit (zT); and (b) efficiency (η) of the pure Cu_2Se and samples made with Na_2CO_3 additions. Some previously reported Cu_2Se data[6] is also shown.

The efficiency of the 1.40 wt.% Na_2CO_3 sample was estimated to be 25% which is ~40% higher than for a pure Cu_2Se sample. Moreover, another crucial factor is the thermoelectric compatibility factor, C_i, defined for each material *i* in an energy-producing thermoelectric device as[42]

$$C_i = \frac{\sqrt{1+(zT)_i}-1}{S_i T} \quad (4)$$

where $(zT)_i$ and S_i are the figure-of-merit and Seebeck coefficient for material *i* respectively. The C_i's of the materials in an energy-producing thermoelectric evoke should be within a factor or two or so, or else efficiency is poor.[42] The temperature dependent thermoelectric compatibility factor is shown in **Figure S7** for the undoped and Na_2CO_3-containing Cu_2Se samples. There are several well-known *n*-type thermoelectric materials so it is easy to select candidates having a compatibility factor which is within the factor of 2 of the Na_2CO_3-containing Cu_2Se samples. Therefore, two of

the most important parameters for thermoelectrics (high *zT* values and similar compatibility factor) can be readily achieved using Cu_2Se made with Na_2CO_3 additions.

3. Discussion

Na_2CO_3 will slowly decompose above its melting point of 1123 K (850 °C).[43] The reactions are $Na_2CO_3 \rightarrow Na_2O\,(s) + CO_2\,(g)$ followed by $Na_2O \rightarrow 2Na\,(g) + \frac{1}{2}O_2\,(g)$. The reactions in pure Na_2CO_3 are 'extremely' slow[43, 44] however it can be appreciated that solution of the product Na and O into the Cu_2Se matrix would lower the activity of these two species and drive the reaction to the right. The present material had been heated to 1473 K which, according to data in the literature, [52,53] should have been associated with about 10 to 20% decomposition in pure Na_2CO_3. Some of the Na and O produced by this decomposition are likely to have been incorporated into the β--Cu_2Se as dopants.

Given the 27 % difference in size between the large Na^+ ion and the small Cu^+ ion,[25] and the significant difference in electronegativity, it is clear that solubility of Na in the $Cu_{2-x}Se$ lattice should be limited, as indeed already pointed out by Zhu et al.[23] This is different to the situation for Pb chalcogenide thermoelectric compounds where Na^+ is about 12% *smaller* than the Pb^{2+} that it replaces, and where of the order an atomic percent solubility has been verified.[27] Nevertheless, if Na is actually taken up into the $Cu_{2-x}Se$ lattice in place of Cu then one would expect to see an inflation of the lattice parameter and, possibly, some effect on the $\alpha \rightarrow \beta$ transition temperature. Whereas Zhu et al.[23] did not find any change in lattice parameter, Jin et al.[24] detected a 5% increase on addition of Na in some samples, but not others. Similarly Sudha et al.[22] found an erratic trend in lattice parameter with Na addition, with smaller additions of Na apparently causing more inflation than larger ones. In contrast, the oxygen ion is 34% *smaller* than Se^{2+}, so substitution of O onto Se sites would normally be expected to cause contraction of the lattice. In

the present work the lattice constants increased as Na_2CO_3 was added up to about 1.40 wt.%, suggesting that substitutional solid-solution alloying of Na is the major factor.

The increased *zT* in these samples is driven by both the decreased thermal conductivity when Na_2CO_3 had been added and the increased electrical conductivity. The latter appears to be most strongly driven by an increase in carrier density associated with the Na_2CO_3 additions. The precise identity of the factors responsible for the decreased thermal conductivity is still unresolved. The fracture surfaces lack the obvious porosity shown in the work of Zhu et al.[23] nor are there prominent second phase inclusions. Therefore, phonon scattering off voids or second phases can be ruled out as a primary factor. The most probable explanation is that the doped Cu_2Se lattice itself is under strain due to the significant mismatch in size between the Na and Cu atoms, and this, together with oxygen substitution for Se, has resulted in increased scattering of the phonons as they propagate through the lattice. The possible additional contribution of dislocations and vacancies should also be investigated in future. In addition, these enhancements to the physical properties of the Cu_2Se lattice can potentially be combined in future with additional improvements from second phase inclusions such as graphite, graphene or boron.[10, 11, 18]

3. Conclusions

Cu_2Se is a relatively well-known thermoelectric compound but provides only modest performance characteristics in its pure form. Here we have shown that the simple step of adding Na_2CO_3 prior to melting and casting bulk Cu_2Se provides a simple and effective means of increasing its performance. The increase is driven by a simultaneous increase in electrical conductivity and a decrease in thermal conductivity. DFT calculations and measurements of Hall carrier concentration strongly indicates that the improved electrical conductivity is the consequence of an increased concentration of *p*-type carriers. DFT calculations suggest that solid solution alloying of both Na and O could cause this. The reason for the decreased thermal conductivity is less clear. Phonon

scattering off voids and second phase inclusions is not likely in the present case as the microstructure of the samples lacks these. Therefore, it seems most probably that the phonon propagation is being hampered by strain in the lattice caused by either or both Na and O atoms that have been taken up into solid solution.

4. Experimental Section

Synthesis: The Cu_2Se powder was mixed with 0.09, 0.18, 0.35, 0.70, and 1.40 wt.% anhydrous sodium carbonate (Sigma-Aldrich, >99.5% purity) powder using a mortar and pestle. Following this samples were heated to ~1473 K in Ar-5 vol.% H_2 flow at a heating rate of 10 K/min, with a 20-minute dwell at 1473 K, followed by furnace cooling to room temperature. Finally, the dense polycrystalline bulks were shaped into round disks and rectangular bar (for thermal and electrical transport measurements, respectively) using a Struers Accutom-50 cutting machine. The sodium carbonate-incorporated samples are denoted by their sodium carbonate weight percent so that the sample with 1.40 wt.% sodium carbonate was denoted as 1.40 Na_2CO_3, etc.

First-principles Calculations: First-principles calculations were performed using density functional theory (DFT)[45] implemented by the Cambridge Serial Total Energy Package (CASTEP). The exchange-correlation functional used is the Generalized Gradient Approximation (GGA) with the Perdew–Burke–Ernzerhof (PBE).[46] Structural optimizations were performed, and the atomic positions and cell vectors were relaxed until the energy, maximum force, and maximum displacement was converged within 5×10^{-6} eV and 0.01 eV/Å and 5×10^{-4} Å respectively. An optimized crystal structure with a lattice parameter of a = 5.8365 Å with the Fm-3m cubic space group was obtained for pure β-Cu_2Se. This is close to the 5.833 Å reported[47] for actual material. The reciprocal space paths selected for the

band structure calculations are the X→R→M→Γ→R through the Brillouin zone of the primitive cell reciprocal space, The conventional and primitive cell band structures calculated are consistent with calculation found in literature.[35]

Crystal Structure: Room temperature X-ray diffraction (XRD) patterns were collected on a Bruker D8 Discover XRD system using Cu Kα radiation to determine the phases and crystal structures. The samples were scanned in the 2θ range of 10–60° with a step of 0.02° and time per step = 1s. The peaks due to Cu K$_\beta$ were attenuated by Ni filter (D5000). The lattice parameters for undoped Cu_2Se and Na_2CO_3 incorporated Cu_2Se were determined by the Rietveld refinement method using Rietica (http://rietica.org/).

Temperature-dependent X-ray Diffraction: High-resolution synchrotron powder diffraction data were collected on the Powder Diffraction beamline at the Australian Synchrotron using λ = 0.58973 Å. Detectors covering an angular range of 2θ = 2.5° were scanned up to 2θ = 80°, simultaneously every 30 seconds, and the sample was rotated at ~1 Hz with a heating rate of 4 deg./min under a helium gas flow over the 300−774 K temperature range. The measured samples were prepared as follows: A piece of the consolidated material with a mass of about 60 mg was chipped of and ground using a mortar and pestle. The resulting powder was transferred into a 0.5 mm outer-diameter quartz capillary tube. The capillary was filled up to about 20 mm in height, and importantly, the powder was tightly packed by vibrating it in a sonicator.

Data Processing: The positions and areas of selected peaks were extracted from X-ray diffraction patterns using FITYK0.9[48] using scripts generated by the same software used to assemble the consecutive synchrotron scans into iso-intensity maps. The 004 (d=6.82 Å) and

139 (d=2.27 Å) peaks are unique to the low temperature α phase and were examined in detail. The areas were normalized to a value of 1.0 at 303 K for purposes of comparison.

Electron Microscopy: Field emission scanning electron microscopy (FE-SEM) (Zeiss EVO SEM) was used to investigate the morphology of pure and samples to which Na_2CO_3 had been added. Transmission electron microscopy (TEM) images were obtained on a FEI Tecnai T20 TEM (LaB6) transmission electron microscope with an accelerating voltage of 200 kV.

TG and DTA: TG–DTA techniques were used to study the decomposition of pure Na_2CO_3. The TG–DTA experiments were carried out in Q600 SDT instrument and rate of temperature increase was 10 K per minute.

Electrical Property: The electrical conductivity and Seebeck coefficient were measured simultaneously under a helium atmosphere from room temp to 984 K using a commercial Ozawa RZ2001i (Japan) instrument. Carrier concentration and carrier mobility were measured by the van der Pauw technique (eZHEMS).

Thermal Conductivity: The thermal diffusivity (*D*) was measured by the laser flash method (Linseis LFA 1000) under vacuum. The specific heat (C_p) was determined by differential scanning calorimetry (DSC) (Netzsch DSC-204F1-Phoenix calorimeter) under an argon atmosphere with a flow rate of 50 ml/min. The samples' densities (*dd*) were calculated using the measured weight and dimensions. The thermal conductivity (κ) was calculated by $\kappa = D \times C_p \times dd.$

Acknowledgments

This work was supported by the Australian Research Council (DP180100645) and an Endeavour

Postdoctoral Research Leadership Award

Supporting Information

Supporting Information is available from the Wiley Online Library or from the author.

Received: ((will be filled in by the editorial staff))
Revised: ((will be filled in by the editorial staff))
Published online: ((will be filled in by the editorial staff))

[1] C. B. Vining, *Nature Mater.* **2009**, *8*, 83.
[2] V. Jovovic, Vol. DE-EE0005387, U.S. Department of Energy, United States **2016**.
[3] A. R. M. Siddique, S. Mahmud, B. V. Heyst, *Renewable and Sustainable Energy Reviews* **2017**, *73*, 730.
[4] Z. Liu, N. Sato, W. Gao, K. Yubuta, N. Kawamoto, M. Mitome, K. Kurashima, Y. Owada, K. Nagase, C.-H. Lee, J. Yi, K. Tsuchiya, T. Mori, *Joule* **2021**, *5*, 1196.
[5] E. F. Hampl, *United States Patent 3,853,632*, **1973**.
[6] H. Liu, X. Shi, F. Xu, L. Zhang, W. Zhang, L. Chen, Q. Li, C. Uher, T. Day, G. J. Snyder, *Nat. Mater.* **2012**, *11*, 422.
[7] S. M. K. N. Islam, P. H. Mayank, Y. Ouyang, J. Chen, A. K. Sagotra, M. Li, M. B. Cortie, R. Mole, C. Cazorla, D. Yu, X. Wang, R. A. Robinson, D. L. Cortie, *Acta Mater.* **2021**, *215*, 117026.
[8] S. M. K. N. Islam, M. B. Cortie, X. Wang, *J. Mater. Chem. A* **2020**, *8*, 16913; Q. Hu, Y. Zhang, Y. Zhang, X.-J. Li, H. Song, *J. Alloys Compounds* **2020**, *813*, 152204.
[9] T. P. Bailey, S. Hui, H. Xie, A. Olvera, P. F. P. Poudeu, X. Tang, C. Uher, *J. Mater. Chem. A* **2016**, *4*, 17225.
[10] L. Zhao, S. M. K. N. Islam, J. Wang, D. L. Cortie, X. Wang, Z. Cheng, J. Wang, N. Ye, S. Dou, X. Shi, L. Chen, G. J. Snyder, X. Wang, *Nano Energy* **2017**, *41*, 164; R. Nunna, P. Qiu, M. Yin, H. Chen, R. Hanus, Q. Song, T. Zhang, M.-Y. Chou, M. T. Agne, J. He, G. J. Snyder, X. Shi, L. Chen, *Energy Environ. Sci.* **2017**, *10*, 1928.
[11] M. Li, D. L. Cortie, J. Liu, D. Yu, S. M. K. N. Islam, L. Zhao, D. R. Mitchell, R. A. Mole, M. B. Cortie, S. Dou, *Nano Energy* **2018**, *53*, 993.
[12] S. D. Kang, S. A. Danilkin, U. Aydemir, M. Avdeev, A. Studer, G. J. Snyder, *New J. Phys.* **2016**, *18*, 013024.
[13] H. Liu, X. Yuan, P. Lu, X. Shi, F. Xu, Y. He, Y. Tang, S. Bai, W. Zhang, L. Chen, *Adv. Mater.* **2013**, *25*, 6607.
[14] D. Byeon, R. Sobota, K. Delime-Codrin, S. Choi, K. Hirata, M. Adachi, M. Kiyama, T. Matsuura, Y. Yamamoto, M. Matsunami, T. Takeuchi, *Nature Comm.* **2019**, *10*, 72.
[15] T. W. Day, K. A. Borup, T. Zhang, F. Drymiotis, D. R. Brown, X. Shi, L. Chen, B. B. Iversen, G. J. Snyder, *Mater. Renew. Sustain. Energy* **2014**, *3*, 26.
[16] A. Olvera, N. Moroz, P. Sahoo, P. Ren, T. Bailey, A. Page, C. Uher, P. Poudeu, *Energy & Environmental Science* **2017**, *10*, 1668.
[17] P. Peng, Z. N. Gong, F. S. Liu, M. J. Huang, W. Q. Ao, Y. Li, J. Q. Li, *Intermetallics*

2016, *75*, 72.
[18] S. M. K. N. Islam, M. Li, U. Aydemir, X. Shi, L. Chen, G. J. Snyder, X. Wang, *J. Mater. Chem. A* **2018**, *6*, 18409.
[19] S. D. Kang, J.-H. Pöhls, U. Aydemir, P. Qiu, C. C. Stoumpos, R. Hanus, M. A. White, X. Shi, L. Chen, M. G. Kanatzidis, G. J. Snyder, *Materials Today Physics* **2017**, *1*, 7.
[20] L. Zhao, F. Y. Fei, J. Wang, F. Wang, C. Wang, J. Li, J. Wang, Z. Cheng, S. Dou, X. Wang, *Scientific Reports* **2017**, *7*, 40436.
[21] L. Yang, Z.-G. Chen, G. Han, M. Hong, L. Huang, J. Zou, *Journal of Materials Chemistry A* **2016**, *4*, 9213.
[22] A. P. Sudha, J. Henry, K. Mohanraj, G. Sivakumar, *Appl. Phys. A* **2018**, *124*, 164.
[23] Z. Zhu, Y. Zhang, H. Song, X. J. Li, *Appl. Phys. A* **2019**, *125*, 572.
[24] Y. Jin, M.-K. Han, S.-J. Kim, Y. Jin, M.-K. Han, S.-J. Kim, *Appl. Sci.* **2018**, *8*, 12.
[25] R. D. Shannon, *Acta Cryst. A* **1976**, *32*, 751.
[26] A. J. Crocker, *J. Phys. Chem. Solids* **1967**, *28*, 1903.
[27] S. A. Yamini, D. R. G. Mitchell, Z. M. Gibbs, R. Santos, V. Patterson, S. Li, Y. Z. Pei, S. X. Dou, G. J. Snyder, *Adv. Energy Mater.* **2015**, *5*, 1501047.
[28] K. Biswas, J. He, I. D. Blum, C.-I. Wu, T. P. Hogan, D. N. Seidman, V. P. Dravid, M. G. Kanatzidis, *Nature* **2012**, *489*, 414.
[29] L. Gulay, M. Daszkiewicz, O. Strok, A. Pietraszko, *Chem. Met. Alloys* **2011**, *4*, 200.
[30] *Alloy Phase Diagrams*, Vol. 3, ASM, Materials Park, Ohio, USA **2016**.
[31] B. Yu, W. Liu, S. Chen, H. Wang, H. Wang, G. Chen, Z. Ren, *Nano Energy* **2012**, *1*, 472.
[32] X. Su, F. Fu, Y. Yan, G. Zheng, T. Liang, Q. Zhang, X. Cheng, D. Yang, H. Chi, X. Tang, *Nature Comm.* **2014**, *5*, 4908; H. Kim, S. Ballikaya, H. Chi, J.-P. Ahn, K. Ahn, C. Uher, M. Kaviany, *Acta Mater.* **2015**, *86*, 247; L. Zhao, X. Wang, J. Wang, Z. Cheng, S. Dou, J. Wang, L. Liu, *Sci. Rep.* **2015**, *5*, 7671; S. Butt, W. Xu, M. U. Farooq, G. K. Ren, Q. Zhang, Y. Zhu, S. U. Khan, L. Liu, M. Yu, F. Mohmed, Y. Lin, C.-W. Nan, *ACS Appl. Mater. Interfaces* **2016**, *8*, 15196; G. Tan, F. Shi, S. Hao, L.-D. Zhao, H. Chi, X. Zhang, C. Uher, C. Wolverton, V. P. Dravid, M. G. Kanatzidis, *Nature Comm.* **2016**, *7*.
[33] D. R. Brown, T. Day, K. A. Borup, S. Christensen, B. B. Iversen, G. J. Snyder, *APL Mater.* **2013**, *1*, 052107; M. Horvatić, Z. Vučić, *Sol. Stat. Ionics* **1984**, *13*, 117.
[34] X. L. Wang, S. X. Dou, C. Zhang, *NPG Asia Mater.* **2010**, *2*, 31; X. L. Wang, *Phys. Rev. Lett.* **2008**, *100*, 156404.
[35] M. Råsander, L. Bergqvist, A. Delin, *J. Phys.: Conden. Matt.* **2013**, *25*, 125503.
[36] L. Zhao, X. Wang, F. F. Yun, J. Wang, Z. Cheng, S. Dou, J. Wang, G. J. Snyder, *Adv. Electron. Mater.* **2015**, *1*, 1400015.
[37] H.-S. Kim, Z. M. Gibbs, Y. Tang, H. Wang, G. J. Snyder, *APL Mater.* **2015**, *3*, 041506.
[38] S. Ballikaya, H. Chi, J. R. Salvador, C. Uher, *J. Mater. Chem. A* **2013**, *1*, 12478; B. Gahtori, S. Bathula, K. Tyagi, M. Jayasimhadri, A. Srivastava, S. Singh, R. Budhani, A. Dhar, *Nano Energy* **2015**, *13*, 36; Y. Pei, X. Shi, A. LaLonde, H. Wang, L. Chen, G. J. Snyder, *Nature* **2011**, *473*, 66.
[39] S. I. Kim, K. H. Lee, H. A. Mun, H. S. Kim, S. W. Hwang, J. W. Roh, D. J. Yang, W. H. Shin, X. S. Li, Y. H. Lee, *Science* **2015**, *348*, 109; Z.-G. Chen, X. Shi, L.-D. Zhao, J. Zou, *Prog. Mater. Sci.* **2018**, *97*, 283.
[40] T. Zhu, Y. Liu, C. Fu, J. P. Heremans, J. G. Snyder, X. Zhao, *Adv. Mater.* **2017**, *29*, 1605884.
[41] H. S. Kim, W. Liu, G. Chen, C.-W. Chu, Z. Ren, *Proc. Nat. Acad. Sci.* **2015**, *112*, 8205.
[42] G. J. Snyder, T. S. Ursell, *Phys. Rev. Lett.* **2003**, *91*, 148301.
[43] J.-W. Kim, H.-G. Lee, *Metall. Mater. Trans. B* **2001**, *32*, 17.
[44] K. Motzfeldt, *J. Phys. Chem.* **1955**, *59*, 139.
[45] P. Hohenberg, W. Kohn, *Phys. Rev.* **1964**, *136*, B864; W. Kohn, L. J. Sham, *Phys. Rev.* **1965**, *140*, A1133.

[46] J. P. Perdew, K. Burke, M. Ernzerhof, *Phys. Rev. Lett.* **1996**, *77*, 3865.
[47] T. Sakuma, K. Sugiyama, E. Matsubara, Y. Waseda, *Mater. Trans. JIM* **1989**, *30*, 365.
[48] M. Wojdyr, *J. Appl. Cryst.* **2010**, *43*, 1126.

The thermoelectric properties of melt-route Cu_2Se are remarkably improved if the material is synthesized with small additions of Na_2CO_3. The improvement is due to a simultaneous increase in electrical conductivity coupled with a decrease in thermal conductivity.

S. Md K. Nazrul Islam, Md R. Rahman, Al J. Ahmed, F. F. Yun, D. L. Cortie, X. Wang*, M. B. Cortie*

Beneficial effect of Na_2CO_3 additions on the thermoelectric performance of melt-route Cu_2Se

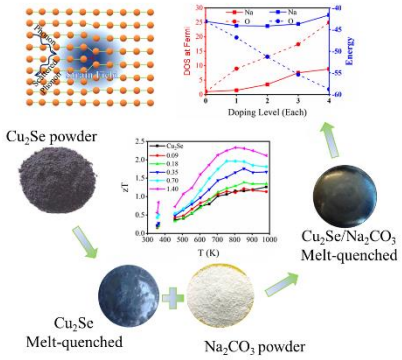

Supporting Information

Beneficial effect of Na_2CO_3 additions on the thermoelectric performance of melt-route Cu_2Se

Sheik Md Kazi Nazrul Islam, Md Rezoanur Rahman, Al Jumlat Ahmed, Frank Fei Yun, David L. Cortie, Xiaolin Wang, Michael B. Cortie**

Table S1. Parameters for the refinement of pure Cu_2Se and Na_2CO_3 incorporated Cu_2Se samples at room temperature. R_p and R_{wp} are the profile and weighted profile R-factors, respectively, χ^2 is the goodness-of-fit, and Derived Bragg R-Factor.

	a (Å)	b (Å)	c (Å)	β (°)	V (Å^3)	R_p	R_{wp}	χ^2	DERIVED BRAGG R-FACTOR
Cu_2Se	7.13304 ± 0.0009	12.36786 ± 0.0014	27.34226 ± 0.0031	94.34507 ± 0.0099	2405.211 ± 0.5035	4.95	6.46	0.06	2.36
0.09 wt.% Na_2CO_3	7.13457 ± 0.0013	12.36909 ± 0.0025	27.34171 ± 0.0055	94.33521 ± 0.0087	2405.952 ± 0.8150	4.63	6.07	0.05	2.00
0.18 wt.% Na_2CO_3	7.13374 ± 0.0010	12.37004 ± 0.0018	27.34909 ± 0.0040	94.34977 ± 0.0084	2406.46 ± 0.6068	4.46	5.82	0.05	2.06
0.35 wt.% Na_2CO_3	7.13345 ± 0.0015	12.37146 ± 0.0028	27.35002 ± 0.0062	94.35077 ± 0.0087	2406.717 ± 0.9100	4.71	6.12	0.05	2.30
0.70 wt.% Na_2CO_3	7.13683 ± 0.0009	12.37408 ± 0.0014	27.37454 ± 0.0031	94.3719 ± 0.0096	2410.457 ± 0.4916	4.76	6.23	0.06	2.51
1.40 wt.% Na_2CO_3	7.13944 ± 0.0010	12.37765 ± 0.0014	27.38372 ± 0.0034	94.37183 ± 0.0101	2412.842 ± 0.5282	4.9	6.37	0.06	2.93

Table S2. Parameters for the refinement of pure Cu_2Se and Na_2CO_3 incorporated Cu_2Se samples at 398 K, 448 K, 498 K, 548 K, 648 K, and 747 K. R_p and R_{wp} are the profile and weighted profile R-factors, respectively, χ^2 is the goodness-of-fit, and Derived Bragg R-Factor.

Temp (K)	Lattice parameter / Sample	a (Å)	R_p	R_{wp}	χ^2	DERIVED BRAGG R-FACTOR
398	1.40 wt% Na_2CO_3	5.8126 ±0.0004	8.58	11.2	1.20	0.96
448		5.8202 ±0.0003	8.68	11.24	1.21	0.75
498		5.8282 ±0.0002	8.95	11.69	1.31	0.54
548		5.8354 ±0.0002	8.52	11.75	1.95	3.44
648		5.8515 ±0.0001	9.9	12.9	1.56	5.34
747		5.8669 ±0.0001	8.88	12	1.98	7.07
397	Cu_2Se	5.8026 ±0.0003	7.58	10.46	1.69	0.71
447		5.8099 ±0.0003	7.78	10.49	1.663	0.83
497		5.8170 ±0.0002	7.91	10.76	1.713	0.89
548		5.8258 ±0.0001	7.51	10.34	2.05	2.61
646		5.8408 ±0.0001	9.42	12.61	2.32	2.63
747		5.8594 ±0.0001	9.76	13.34	2.538	3.35

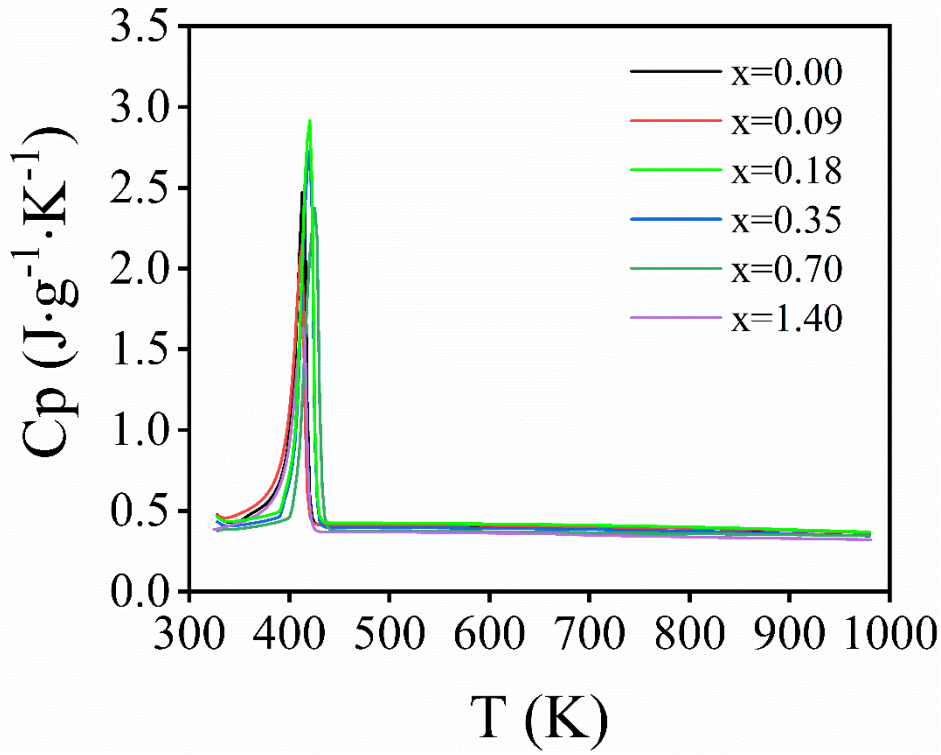

Figure S1. Temperature dependence of heat capacity (C_p) for different additions of Na_2CO_3 to Cu_2Se.

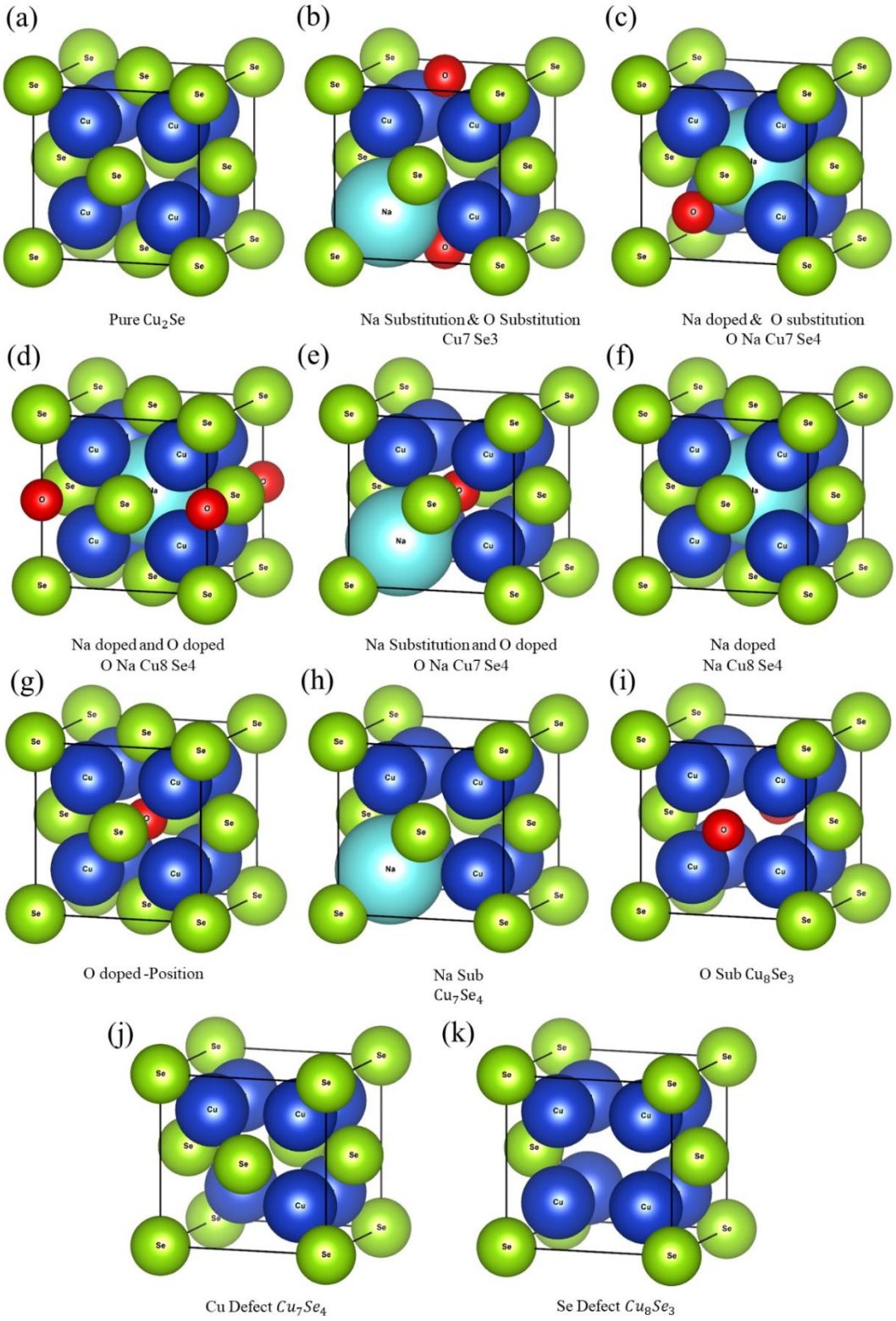

Figure S2. Unit cell of (a) stoichiometric Cu_2Se; (b) Na O Cu_7 Se_3 (Na Substitution and O Substitution); (c) O Na Cu_7 Se_4 (Na doped and O substitution); (d) O Na Cu_8 Se_4 (Na doped and O doped); (e) O Na Cu_7 Se_4 (Na Substitution and O doped); (f) Na Cu_8 Se_4 (Na doped); (g) O Cu_8 Se_4 (O doped); (h) Na Cu_7 Se_4 (Na substitute); (i) O Cu_8 Se_3 (O substitute); (j) Cu_7 Se_4 (Cu defect); (k) Cu_8 Se_3 (Se defect); (l) Cu_8 Se_4 (Na_2O defect).

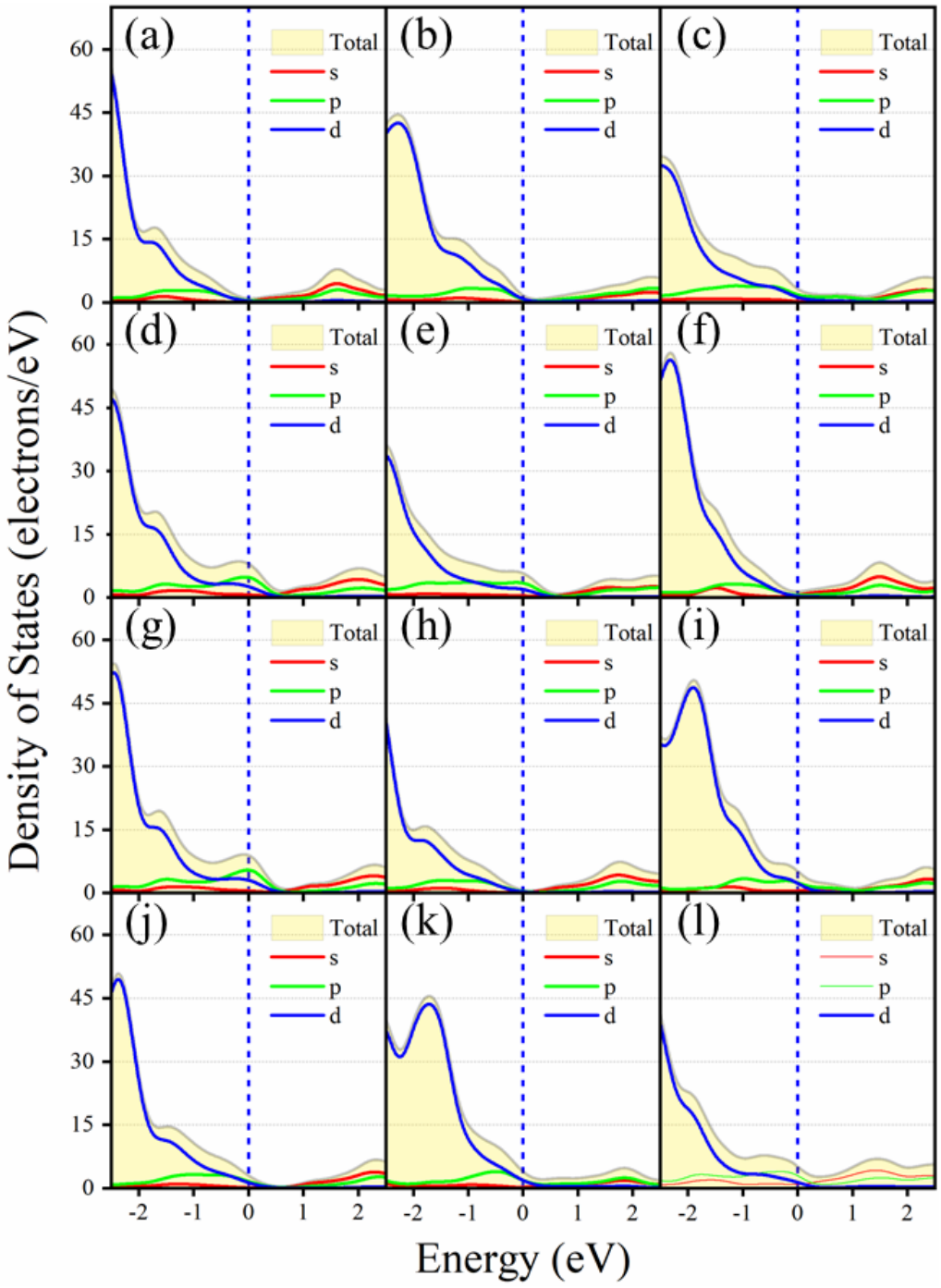

Figure S3. Calculated total and partial electronic density of states (DOS) for the stoichiometric Cu_2Se and Cu_2Se with Na and/or O compounds obtained from the Density Functional Theory calculations. (a) total and partial DOS for the Cu_2Se; (b) total and partial DOS for the Na O Cu_7 Se_3 (Na Substitution and O Substitution); (c) total and partial DOS for the O Na Cu_7 Se_4 (Na doped and O substitution); (d) total and partial DOS for the O Na Cu_8 Se_4 (Na doped and O doped); (e) total and partial DOS for the O Na Cu_7 Se_4 (Na Substitution and O doped); (f) total and partial DOS for the Na Cu_8 Se_4 (Na doped); (g) total and partial DOS for the O Cu_8 Se_4 (O doped); (h) total and partial DOS for the Na Cu_7 Se_4 (Na substitute); (i) total and partial DOS for the O Cu_8 Se_3 (O substitute); (j) total and partial DOS for the Cu_7 Se_4 (Cu defect); (k) total and partial DOS for the Cu_8 Se_3 (Se defect); (l) total and partial DOS for the Cu_8 Se_4 (Na_2O defect). The vertical lines mark the position of the Fermi level (E_F)

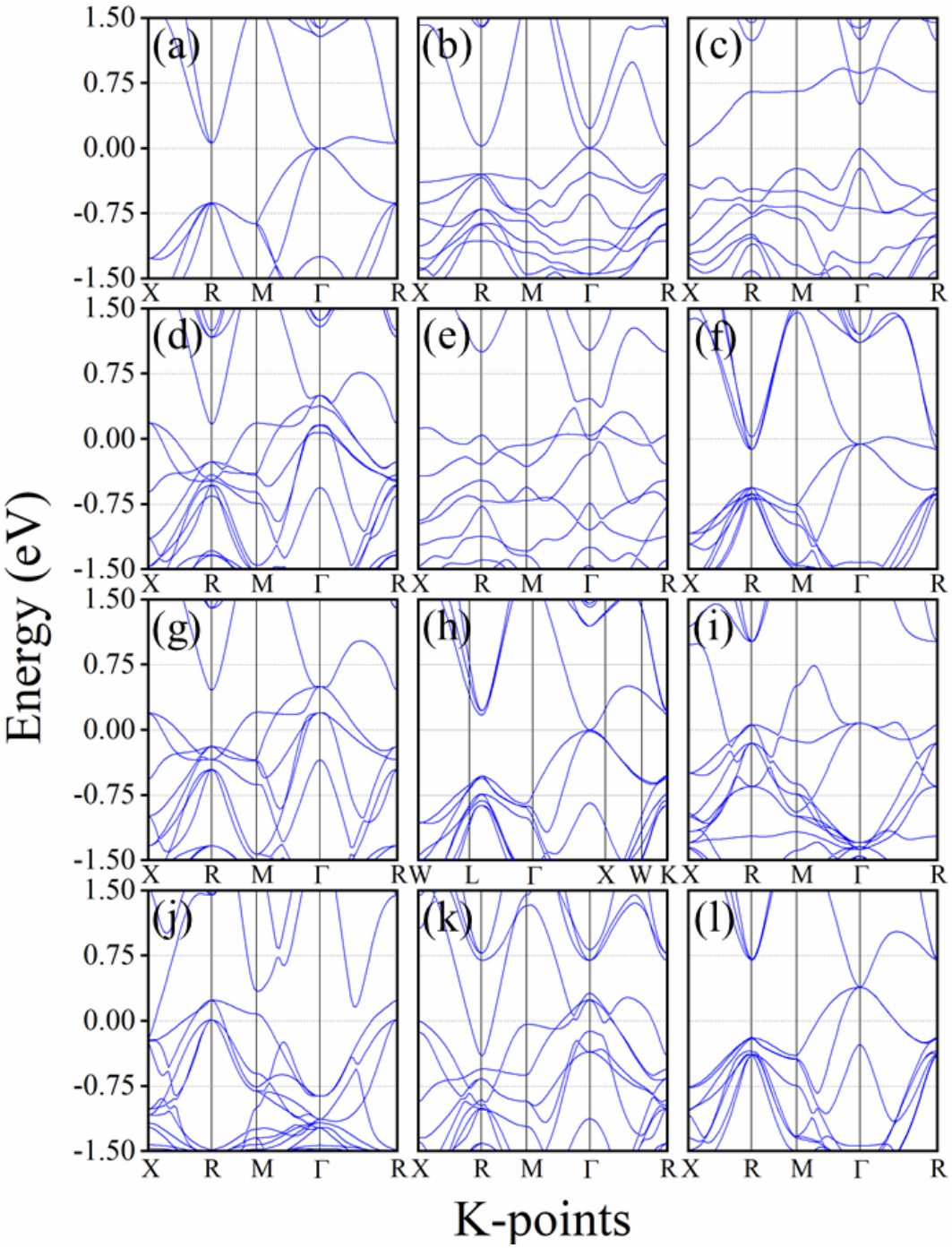

Figure S4. Calculated band structure for the stoichiometric Cu_2Se and Cu_2Se with Na and/or O compounds obtained from the Density Functional Theory calculations. (a) Calculated band structure for the Cu_2Se; (b) Calculated band structure for the Na O Cu_7 Se_3 (Na Substitution and O Substitution); (c) Calculated band structure for the O Na Cu_7 Se_4 (Na doped and O substitution); (d) Calculated band structure for the O Na Cu_8 Se_4 (Na doped and O doped); (e) Calculated band structure for the O Na Cu_7 Se_4 (Na Substitution and O doped); (f) Calculated band structure for the Na Cu_8 Se_4 (Na doped); (g) Calculated band structure for the O Cu_8 Se_4 (O doped); (h) Calculated band structure for the Na Cu_7 Se_4 (Na substitute); (i) Calculated band structure for the O Cu_8 Se_3 (O substitute); (j) Calculated band structure for the Cu_7 Se_4 (Cu defect); (k) Calculated band structure for the Cu_8 Se_3 (Se defect); (l) Calculated band structure for the Cu_8 Se_4 (Na_2O defect).

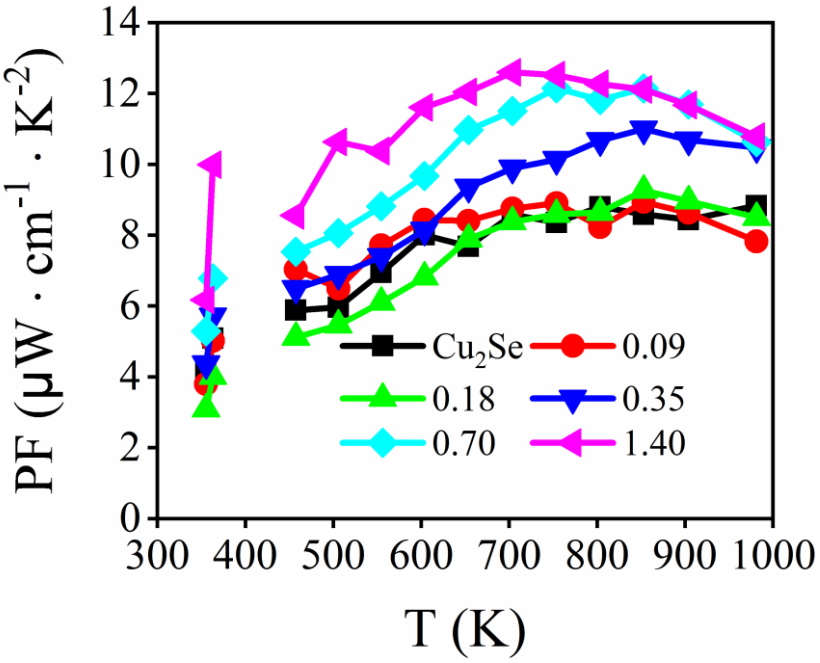

Figure S5. Temperature dependent power factor of the $Cu_2Se-x\text{wt.}\%\ Na_2CO_3$ samples (x = 0, 0.09, 0.18, 0.35, 0.70, and 1.40.

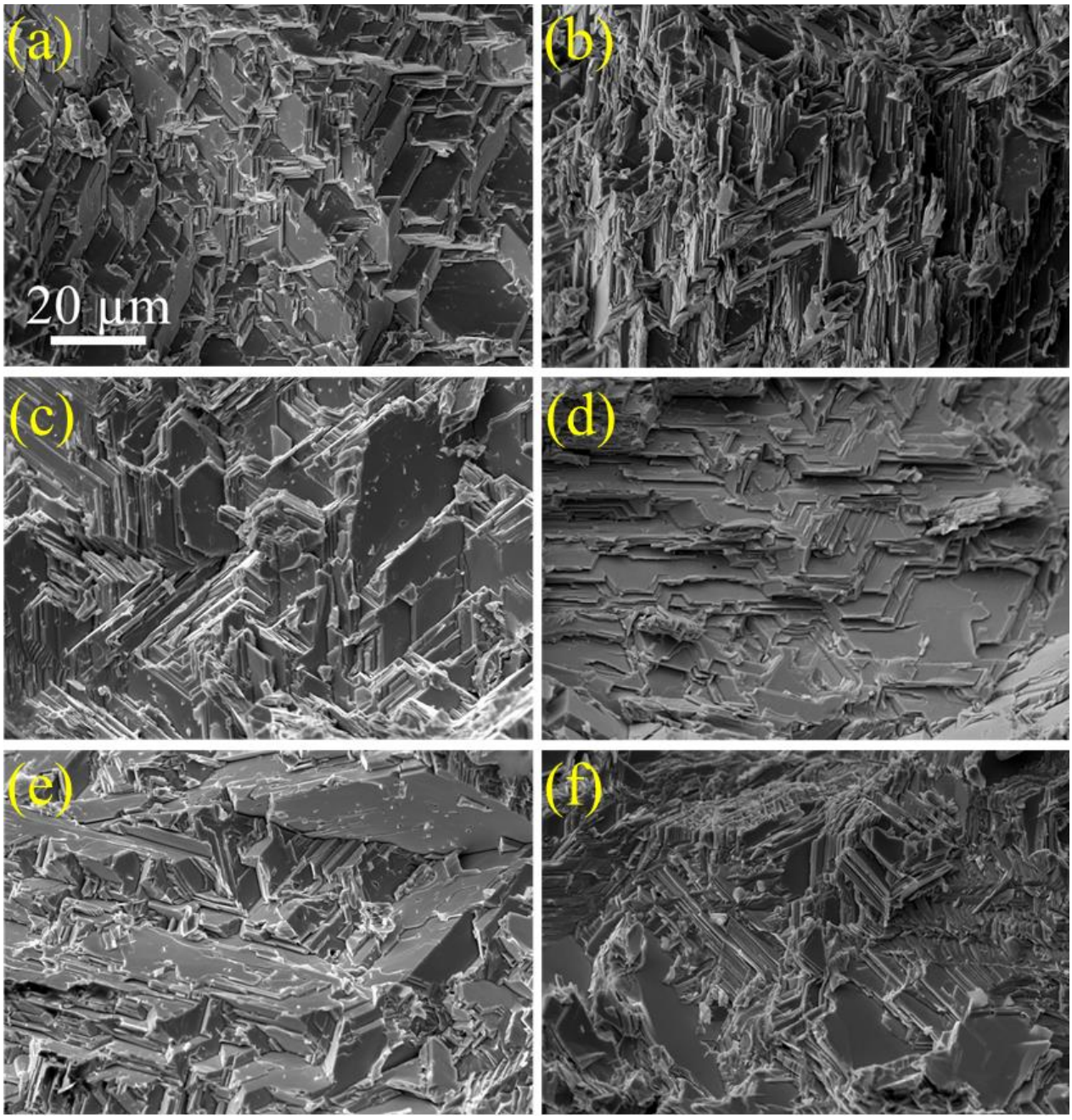

Figure S6. Freshly fractured cross sectioned image of (a) pure Cu_2Se; (b) 0.09 wt.% Na_2CO_3; (c) 0.18 wt.% Na_2CO_3; (d) 0.35 wt.% Na_2CO_3; (e) 0.70 wt.% Na_2CO_3 and (f) 1.40 wt.% Na_2CO_3 samples.

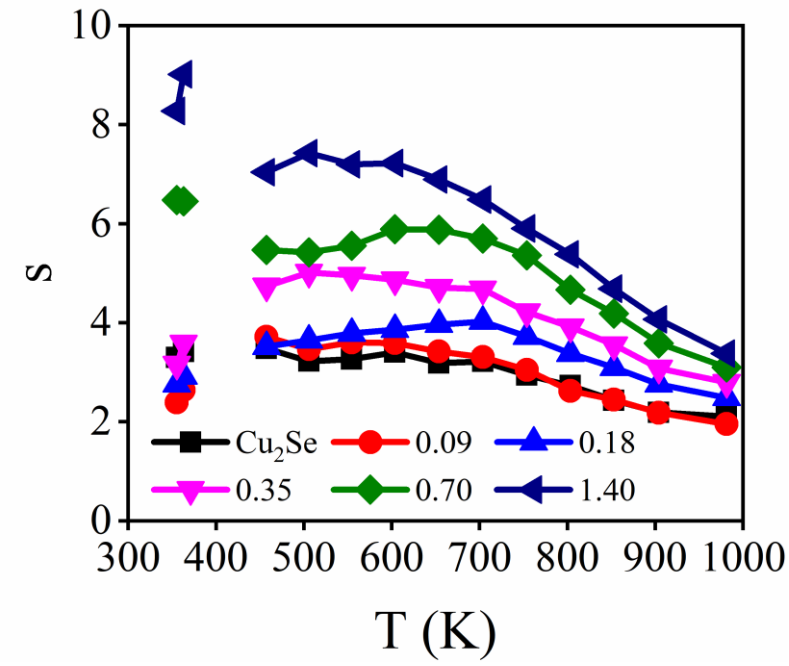

Figure S7. Temperature dependent compatibility factors of the Cu_2Se-*x* wt.% Na_2CO_3 samples (*x* = 0, 0.09, 0.18, 0.35, 0.70, and 1.40).